Article

Modulating Diffusion Double Layer by In Situ Constructed Ultrathin Dipole Layer Towards Uniform Lithium Deposition

Yang Nan [1,2], Songmei Li [2], Wen Li [1,2,*], Guoke Wei [1] and Bin Li [2,*]

1   Aviation Key Laboratory of Science and Technology on Advanced Surface Engineering, AVIC Manufacturing Technology Institute, Beijing 100024, China; weigk@avic.com (G.W.)
2   School of Materials Science and Engineering, Beihang University, Beijing 100191, China
*   Correspondence: liw162@avic.com (W.L.); li_bin@buaa.edu.cn (B.L.)

Abstract: The popularization of lithium metal anode has been limited due to uneven deposition processes and lithium dendrites. Guiding homogeneous nucleation during the initial plating stage of lithium is vital to obtain a stable lithium metal anode. Herein, an ultra-thin dipole layer that can be used to regulate the diffusion layer is prepared by anodizing and strong polarization on a titanium foil collector. It is demonstrated that the vertical distributions of ionic concentration and electrostatic potential on the nBTO@Ti electrode are modulated by the ultrathin dipole layer, leading to uniform diffusion of lithium ions and reduction of overpotential. Consequently, a uniform lithium nucleation and plating process are achieved on a polarized $BaTiO_3$ collector, which is verified by microscopy. The average coulombic efficiency of the deposition-dissolution process is as high as 98.3% for 300 cycles at 0.5 mA cm^{-2}. Moreover, the symmetrical cell shows flat potential platforms of 25 mV for 1000 cycles at 0.5 mA cm^{-2}. Full cell with LiFePO$_4$ as cathode also reveals excellent electrochemical performances with a steady discharge capacity of 120 mAh g^{-1} at 1 C and a high capacity retention of 93.3% after 200 cycles.

Keywords: lithium metal anode; diffusion double layer; lithium dendrites; dipole; lithium battery

1. Introduction

Lithium metal is one of the best anode materials for advanced lithium batteries due to its high theoretical specific capacity (3860 mAh g^{-1}), low density (0.53 g cm^{-3}), and lowest electrode potential (-3.04 V vs. SHE) [1–3]. Unfortunately, lithium metal electrodes are still far from application because of the notorious uncontrolled lithium deposition and formation of dead Li, which brings potential safety risks and continuous degradation of electrochemical performance [4–7]. Generally speaking, the lithium deposition process can be roughly divided into three steps: generation of solid electrolyte interphase (SEI) film, lithium deposition nucleation, and continuous deposition growth. To achieve controlled lithium deposition, a great deal of work has gone into developing artificial SEI films [8,9], guiding homogeneous lithium nucleation [10–12], and developing three-dimensional (3D) electrodes [13,14]. Since the subsequent growth behavior of lithium is largely up to the initial nucleation stage, guaranteeing the homogeneousness of nucleation is crucial [15,16].

The lithium deposition nucleation process is affected by electrochemical factors, which are mainly electrochemical parameters and potential distribution on the electrode surface [17,18]. Various strategies are proposed to regulate lithium nucleation [19–23], such as prefabricated nucleation sites, regularizing current distribution, designing 3D current collectors, and employing concentrated electrolytes. In previous work, a functional SEI film composed of polarized BaTiO$_3$ dipole in a tough polyacrylonitrile matrix was proposed to regulate lithium-ion flux via the piezoelectric effect [8]. As the most direct means, the types and properties of prefabricated nucleation sites on electrodes have been studied in more depth. Lithiophilic nanoparticles or atomic groups are carefully introduced on the surface of the electrodes or into current collectors [24–27]. For example, gradient-distributed

lithiophilic ZnO particles were introduced into the carbonized polyacrylonitrile framework to achieve the stable plating process of lithium [28]. Nevertheless, these strategies have not paid attention to the intrinsic effect of electrode substrate on the diffusion of Li-ions in electrolytes. The key to uniform nucleation is to control the uniform distribution of Li-ions in the diffusion layer of the electrode substrate. Meanwhile, the nucleation barrier of lithium on the electrode should be properly reduced to promote nucleation efficiency.

Herein, a polarized $BaTiO_3$ dipole layer is proposed as a collector to regulate the lithium nucleation process. The electronegativity of polarized $BaTiO_3$ dipoles can attract positive Li-ions in electrolytes and modify the diffused double layer on the polarized $BaTiO_3$ collector, leading to uniform nucleation and deposition of lithium. Simulation results of finite element modeling further prove that Li-ions are enriched near polarized $BaTiO_3$ electrodes. As a result, the overpotential of lithium nucleation is markedly reduced on account of polarized $BaTiO_3$ dipoles, and a high average coulombic efficiency of 98.3% for 300 cycles at 0.5 mA cm^{-2} is achieved during the deposition–dissolution process. Uniform lithium nucleation and stable plating process are verified by observing different deposition stages via micro perspective. The obtained nBTO@Ti/Li anode exhibits stable potential platforms of 25 mV for 1000 h at 0.5 mA cm^{-2} in symmetrical cells. In addition, nBTO@Ti/Li-LiFePO$_4$ full cell possesses a steady discharge capacity of 120 mAh g^{-1} at 1 C and a capacity retention of 93.3% after 200 cycles.

2. Experimental Section

2.1. Preparation of Polarized $BaTiO_3$ Foil

The preparation of polarized $BaTiO_3$ foil can be divided into the following three steps:

(1) Anodization process: A mixture of mixed acid with 200 g/L of H_2SO_4 and 60 g/L of HCl was prepared. Ti foil (50 μm in thickness) and Cu foil acted as anode and cathode, respectively. Ti foil was double folded, and the edges were sealed to ensure that only the outside surface of the Ti foil was anodized. The anodization process was carried out via DC power at 10 V for 10 min. After anodization, a TiO_2 film was generated on the surface of Ti foil according to Formula (1) (labeled as TiO_2@Ti foil) [29].

$$Ti + 2H_2O \rightarrow TiO_2 + 2H_2 \tag{1}$$

(2) Hydrothermal process: The obtained TiO_2@Ti foil was immersed in saturated $Ba(OH)_2$ solution and sealed in a high-pressure reactor. The reactor was heated under 180 °C for 12 h with subsequent natural cooling. During the hydrothermal process, a $BaTiO_3$ film was formed, as illustrated in Formula (2), and the obtained sample was labeled as BTO@Ti foil.

$$TiO_2 + Ba(OH)_2 \rightarrow BaTiO_3 + H_2O \tag{2}$$
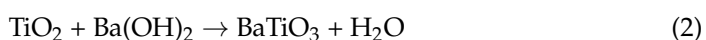
(3) Polarization process: The electric domains in $BaTiO_3$ film can be oriented via the polarization of a strong electrostatic field, while the direction of dipolarity is opposite to that of the electrostatic field [30]. The obtained BTO@Ti foil was cut into two pieces along the folded edge and then covered with insulating polyethylene film (80 μm in thickness). Two stainless-steel sheets were used to clamp the BTO@Ti foil and polyethylene film. Then, an electrostatic field of 50 kV/mm was applied to the stainless-steel sheets for 10 min. The polarized BTO@Ti foil was recorded as nBTO@Ti or pBTO@Ti foil when the negative or positive side of the $BaTiO_3$ dipole was outward, respectively.

2.2. Electrochemical Tests

CR2032 cells (Taiyuan Lizhiyuan Battery Company, Taiyuan, China) with a piece of polypropylene (PP) membrane and about 40 μL commercial electrolyte were assembled for electrochemical tests. Half cells were assembled with the prepared foils (nBTO@Ti, BTO@Ti, and Ti) and pure lithium metal electrodes. The discharge termination condition of half cells during coulombic efficiency (CE) test is set at a discharge capacity of 0.5 mAh cm^{-2},

and the charge termination condition is set at a voltage of 0.5 V. Lithium anodes were obtained by plating 5 mAh cm^{-2} of lithium at 0.5 mA cm^{-2} on nBTO@Ti, BTO@Ti and Ti electrodes, and the corresponding anodes are denoted as nBTO@Ti/Li, BTO@Ti/Li and Ti/Li, respectively. Symmetrical cells were assembled with nBTO@Ti/Li, BTO@Ti/Li, or Ti/Li. EIS tests of symmetrical cells after 10 cycles were performed at an amplitude of 10 mV with frequencies from 100 kHz to 0.1 Hz. Li-LiFePO$_4$ full cells were assembled with LiFePO$_4$ as cathode and nBTO@Ti/Li, BTO@Ti/Li, or Ti/Li as anode.

All the electrochemical tests were carried out via a LANHE electrochemical testing system. The electrolyte type used in Li-LiFePO$_4$ full cells was LB-092, while LS-002 electrolyte was applied in other situations of this work. The above two types of electrolytes were both purchased from DoDoChem (Suzhou, China). The formula of LB-092 is 1M LiPF$_6$ in DMC: EC: EMC = 1:1:1 Vol% with 1%VC, while the formula of LS-002 is 1M LiTFSI in DME: DOL = 1:1 Vol% with 1%LiNO$_3$. As an ester electrolyte, LB-092 possesses more stable electrochemical properties and is suitable for Li-LiFePO$_4$ full cells. However, the conductivity of LB-092 is inferior to that of LS-002 (ether electrolyte). In order to enhance the experimental reproducibility, LS-002 electrolytes were applied in other situations in this work.

2.3. Simulation of Finite Element Modeling

The diffusion double layer structure of the nBTO@Ti electrode surface without applied potential was simulated via the Gouy–Chapman–Stern model by running COMSOL Multiphysics. The diffusion coefficients of cation and anion in electrolyte were set at 1×10^{-9} m^2 s^{-1}, and the bulk concentration of cation and anion was set at 1 mol L^{-1} (1 M). The charge numbers of cations and anions are +1 and −1, respectively, and the temperature of the simulation process was fixed at 298.15 K.

3. Results and Discussions

The principle of directed dipole layer-induced uniform lithium nucleation and the subsequent plating process is illustrated in Figure 1. When the negative side of the dipole film is outward, positively charged lithium ions in the electrolyte will be adsorbed on the electrode surface due to the electrostatic field. Electric double layers are generated instantaneously, and the Li-ion concertation near the electrode surface is higher than that in bulk electrolytes. Such a structure can promote the uniform nucleation of lithium in the initial stage of electrodeposition and the subsequent even deposition of lithium. In contrast, the nucleation of lithium is stochastic without the attractive interaction of lithium, which leads to an inhomogeneous plating process of lithium, even lithium dendrites.
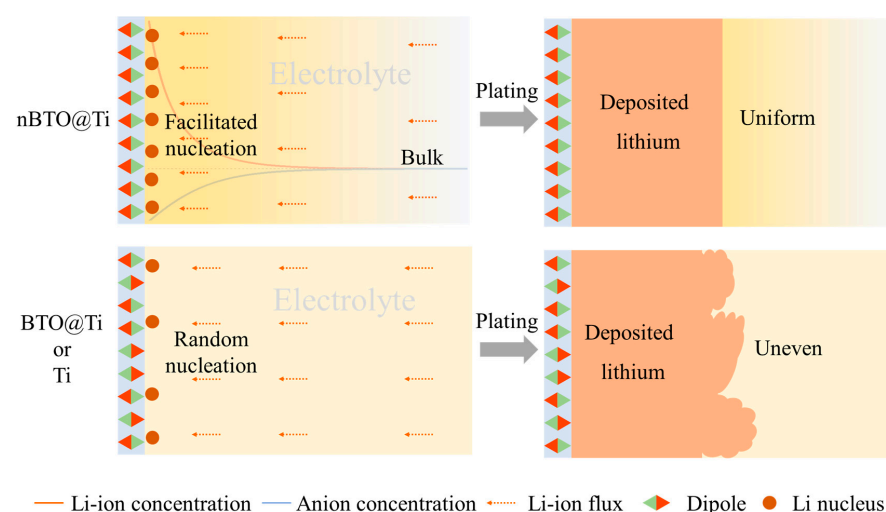

Figure 1. The schematic diagram of diffused double layer induced by BTO dipole layer towards uniform Li-ion flux and lithium deposition.

A diagram of the preparation process of the polarized BTO dipole layer is shown in Figure 2a, which can be divided into three steps: anodization, hydrothermal, and polarization. The surface of Ti foil is transformed into TiO_2 during the anodization process and then $BaTiO_3$ during the hydrothermal process. Afterward, the randomly oriented BTO dipoles in the BTO layer are arranged directly in a strong electrostatic field. Photos of the obtained TiO_2@Ti foil and BTO@Ti foil are shown in Figure S1. After anodizing, the color of the Ti foil changes from silver to gold, while the unsubmerged part of the Ti foil keeps its original color. A blue surface is present ultimately when TiO_2 film is transformed into BTO film during the hydrothermal process. Scanning electron microscope (SEM) and energy dispersive spectrometer (EDS) were applied to study the morphologies and element distributions of the obtained TiO_2@Ti foil and BTO@Ti foil. As shown in Figures 2b and S2, the BTO@Ti foil and TiO_2@Ti foil exhibit smooth morphologies and uniform distributions of elements. The sectional SEM image of the BTO@Ti foil reveals a thin $BaTiO_3$ film of about 190 nm (Figure 2c). To further verify the constituents of $BaTiO_3$ film, X-ray diffraction (XRD) and X-ray photoelectron spectroscopy (XPS) were conducted. As shown in Figure 2d, except for the diffraction peaks of Ti (JCPDS No. 44-1294), extra XRD peaks located at 22.3°, 31.6°, 45.4°, and 56.3° are corresponding to (100), (110), (200), and (211) crystal faces of $BaTiO_3$ (JCPDS No. 05-0626) [31]. The XPS peaks located at 778.64 eV and 739.90 eV in Figure S3a are respectively assigned to Ba $3d_{3/2}$ and Ba $3d_{5/2}$, and the characteristic peaks of Ti $2p_{1/2}$ and Ti $2p_{3/2}$ are verified by the peaks located at 463.93 eV and 458.14 eV in Figure S3b [32–34]. Peaks located at 529.21 eV, 531.08 eV, and 532.40 eV in High-resolution O 1s XPS spectra of BTO@Ti foil are, respectively, assigned to lattice oxygen, adsorbed oxygen and carbonates (Figure S3c) [35].
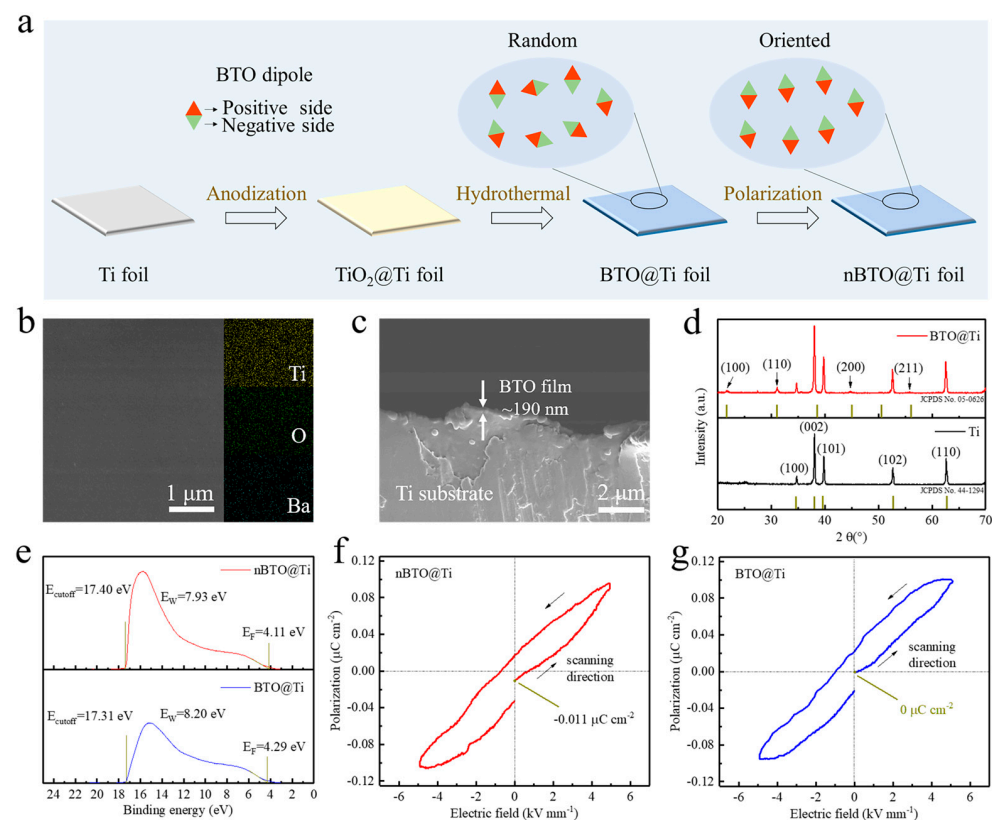

Figure 2. (**a**) Diagram of the preparation process of polarized BTO dipole layer. (**b**) SEM image and EDS mappings of the obtained BTO foil. (**c**) Sectional SEM image of BTO@Ti foil. (**d**) XRD patterns of BTO@Ti foil and Ti foils. (**e**) UPS patterns of BTO@Ti foil and nBTO@Ti foil. Ferroelectric hysteresis loops of (**f**) nBTO@Ti foil and (**g**) BTO@Ti foil.

Since the surface work function (E_w) of BTO@Ti foil is affected by the orientation of the dipoles [36–38], ultraviolet photoelectron spectroscopy (UPS) was measured to confirm the orientation of BaTiO$_3$ dipoles. The E_w of BTO@Ti foil is connected to the orientation of BaTiO$_3$ dipoles, and it can be calculated using Formula (3).

$$E_w = hv - (E_{cutoff} - E_F) \tag{3}$$

where hv is the energy of the ultraviolet photoelectron (He I, 21.22 eV), E_{cutoff} is the cutoff energy of the secondary electron, and E_F is the Fermi level of the instrument. According to the UPS results (Figure 2e), the E_w of BTO@Ti foil without polarization is 8.20 eV. When the negative side of the BaTiO$_3$ dipole is outward, the E_w of nBTO@Ti foil decreases to 7.93 eV. On the other hand, the E_w of pBTO@Ti foil increases to 8.36 eV when the positive side of BaTiO$_3$ dipoles is outward (Figure S4). The ferroelectric hysteresis loop was tested to further verify the dipolarity of nBTO@Ti foil. As demonstrated in Figure 2f, nBTO@Ti foil exhibits polarization intensity of -0.11 µC cm^{-2} when the extra electric field is zero, which can be attributed to the directed BaTiO$_3$ dipoles. Meanwhile, the polarization intensity of unpolarized BTO@Ti foil is zero without an extra electric field (Figure 2g). The variation trends of polarization intensity with extra electric field in Figure 2f,g are similar, which can be ascribed to the substantive characteristic of BaTiO$_3$ dipoles.
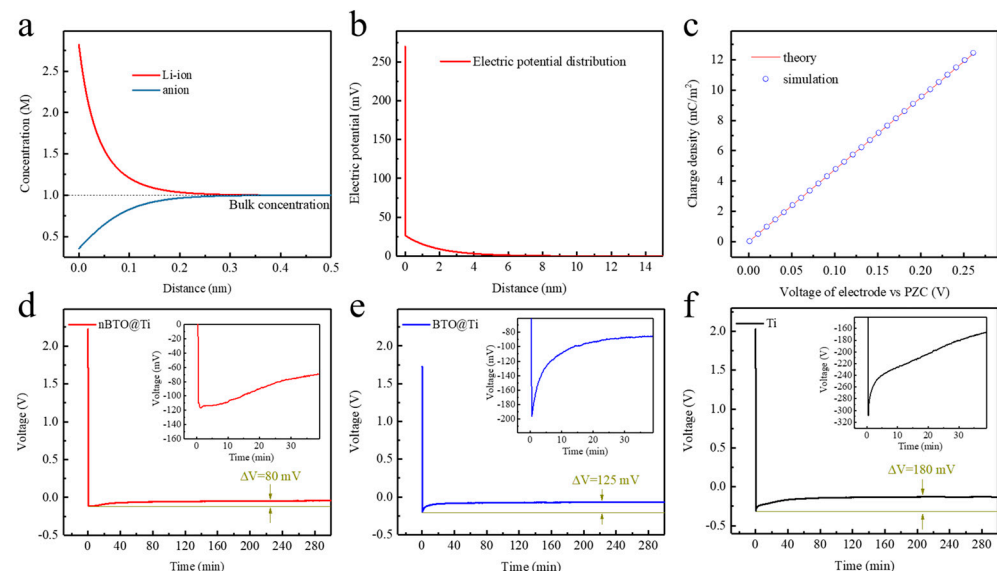

Figure 3. (**a**) Vertical distribution of ionic concentration on nBTO@Ti electrode in the electrolyte. (**b**) Vertical variation of the electrostatic potential on nBTO@Ti electrode in the electrolyte. (**c**) Variation of surface charge density with the potential difference between the electrode and bulk electrolyte. Voltage–time curves of lithium plating process at 0.5 mA cm^{-2} on (**d**) nBTO@Ti, (**e**) BTO@Ti, and (**f**) Ti electrodes.

The electric double-layer structure on the surface of the nBTO@Ti electrode was simulated by COMSOL Multiphysics, and the results are shown in Figure 3a–c. Referring to the difference of E_w between nBTO@Ti foil and BTO@Ti foil, the extra electrostatic potential of nBTO@Ti electrode was set at 0.27 V. As shown in Figure 3a, the concentration of Li-ions near nBTO@Ti foil electrode could reach up to 2.7 M, due to the electrostatic attraction of BaTiO$_3$ dipoles. On the other hand, anions in the electrolyte are repelled, and the relevant concentration decreases to about 0.4 M. Vertical variation of the electrostatic potential on the nBTO@Ti electrode in the electrolyte is expounded in Figure 3b. Electrostatic potential begins to decay rapidly from 270 mV to 25 mV and then slowly decreases with the increase of distance. About 6 nm away from the surface of the nBTO@Ti electrode, the electrostatic potential is approximate to zero. Figure 3c shows the variation of surface charge density with the potential difference between the electrode and the bulk solution,

and it can be seen that the simulation results are highly consistent with the theoretical results. To evaluate the effect of the extra electrostatic potential on the initial nucleation of lithium, voltage–time curves of the lithium plating process at 0.5 mA cm^{-2} on nBTO@Ti, BTO@Ti, and Ti electrodes were measured. The overpotential of lithium nucleation on the nBTO@Ti electrode is 80 mV (Figure 3d), which is 45 mV lower than that of the BTO@Ti electrode (Figure 3e). It indicates that the extra electrostatic potential can significantly reduce the energy barrier of lithium nucleation. The overpotential of lithium nucleation on the Ti electrode is 180 mV, which is observably higher than those of the BTO@Ti and nBTO@Ti electrodes.

To further investigate the electrodeposition behavior of lithium on the nBTO@Ti electrode, different plating periods at 0.5 mA cm^{-2} were observed via SEM. In the initial nucleation phase with a deposition capacity of 0.1 mAh cm^{-2} (as showed in Figure 4(a2,a3)), the lithium metal nuclei are about 1 μm in diameter without stack, and most of the nBTO@Ti electrode surface is covered by uniformly distributed lithium nuclei. The electrostatic attraction of BaTiO$_3$ dipoles reduces the energy barrier of lithium nucleation and enhances the concentration of Li-ions near the nBTO@Ti foil electrode. As a result, the lithium nucleation process on nBTO@Ti is promoted, and uniformly distributed lithium nuclei are also achieved. Such a uniform and encouraging nucleation process of lithium lays the foundation of an even plating process. In the subsequent deposition process (Figure 4(a4,a5)), lithium metal continues to plate along the existing or newly formed lithium metal nuclei, and the entire surface of the nBTO@Ti electrode is gradually uniformly covered by plated lithium. In contrast, only half of the BTO@Ti electrode surface is covered by lithium metal nuclei at a deposition capacity of 0.1 mAh cm^{-2}, and the nuclei exhibit disorganized and partially stacked morphologies (Figure 4(b2,b3)). Without adjusting the Li-ions flow around the electrode, the nucleation process of lithium is chaotic and repressed. As a result, numerous protrusions are generated on the surface of deposited lithium metal (Figure 4(b4,b5)). Under similar conditions, the plated lithium on the Ti electrode appears like moss at a deposition capacity of 0.1 mAh cm^{-2}, revealing an uneven nucleation process (Figure 4(c2,c3)). Eventually, the deposited lithium metal demonstrates a rugged morphology with slumping dendrites (Figure 4(c4,c5)).
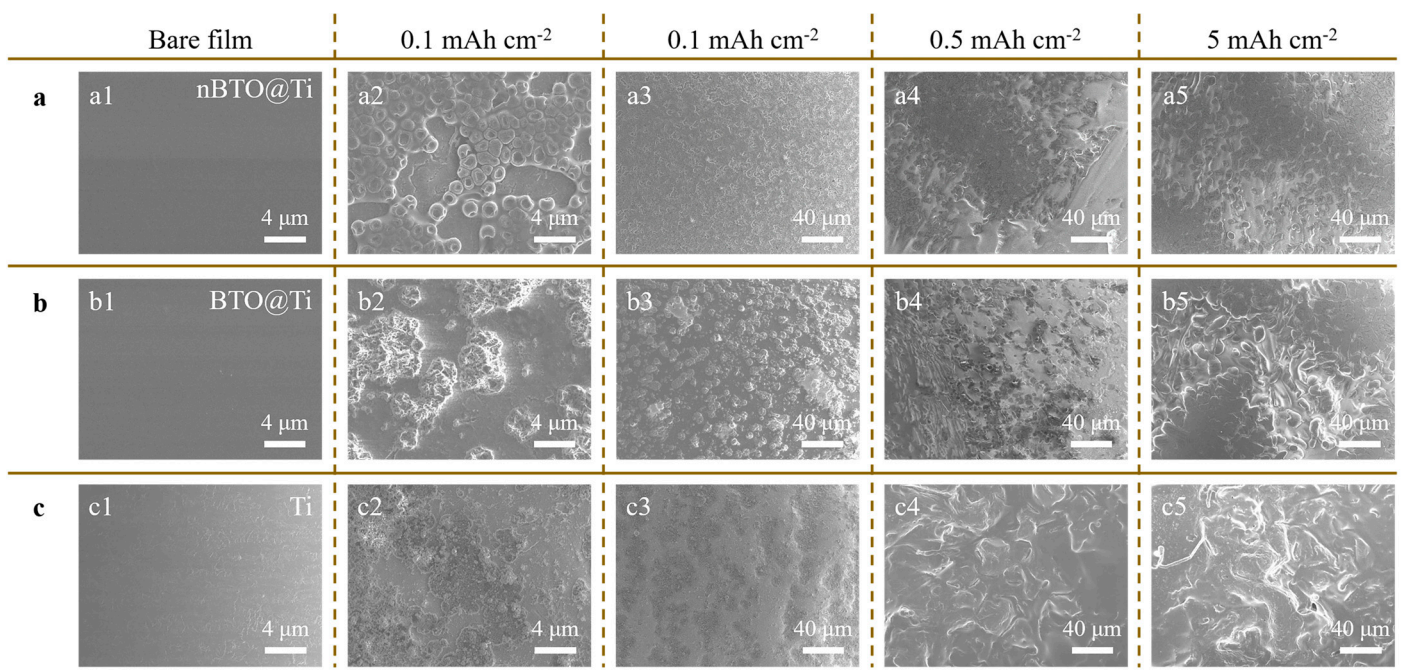

Figure 4. SEM images of (**a**) nBTO@Ti, (**b**) BTO@Ti, and (**c**) Ti electrodes. (**a1,b1,c1**) Bare films. Electrodes with deposited lithium of (**a2,a3,b2,b3,c2,c3**) 0.1 mAh cm^{-2}, (**a4,b4,c4**) 0.5 mAh cm^{-2}, and (**a5,b5,c5**) 5 mAh cm^{-2}.

To assess the stability of the deposition/dissolution process of lithium on the nBTO@Ti electrode, the CE of half-cell with lithium metal as another electrode was measured. A high average CE of 98.3% is achieved during 300 cycles at 0.5 mA cm^{-2} (Figure 5a). In sharp contrast, the CEs of BTO@Ti and Ti electrodes begin to fluctuate sharply after 120 and 100 cycles, respectively. When the applied current density is increased to 1 mA cm^{-2}, the CE of the nBTO@Ti electrode slightly drops to 97.4% during 200 cycles, while the CEs of BTO@Ti and Ti electrodes keep swinging acutely (Figure 5b). Lithium anodes were obtained by plating 5 mAh cm^{-2} of lithium at 0.5 mA cm^{-2} on nBTO@Ti, BTO@Ti, and Ti electrodes, and symmetrical batteries were assembled to evaluate the cycle performance of lithium anodes at constant current densities. Under the influence of the BaTiO$_3$ dipole layer, the obtained nBTO@Ti/Li possesses the flattest morphology. As a result, a symmetrical battery exhibits flat potential platforms of ~25 mV at 0.5 mA cm^{-2} and maintains a stable cycle process for 1000 h when nBTO@Ti/Li is applied (Figure 5c). By contrast, the potential platforms of BTO@Ti/Li-BTO@Ti/Li battery are more volatile with a higher value of ~35 mV. Sharply increased potential after 600 h of cycling manifests the failure of a symmetrical battery. The Ti/Li-Ti/Li battery shows the most volatile potential platforms and fails at 550 h. To further study the kinetics and thermodynamics of the plating/stripping process of Li, the potential platforms of the symmetrical batteries in different stages are enlarged and shown in Figure S5. At the initial cycles, the shapes of the potential platforms are similar to the peak, which can be attributed to transitions between different kinetic pathways at the electrode/electrolyte interphase [39]. The maximum potentials are also reduced and increased because of the increasing active surface area at this stage. After extended cycles (such as the 290th cycle), the shapes of the potential platforms of BTO@Ti/Li-BTO@Ti/Li and Ti/Li-Ti/Li batteries turn into an arch. Such phenomenon can be ascribed to the accumulation of dead Li during cycles [39], which also brings about the subsequent failure of batteries. Due to the uniform surface caused by the polarized BaTiO$_3$ layer, the BTO@Ti/Li-BTO@Ti/Li battery exhibits flat and stable potential platforms. EIS spectrums of the symmetric cells after 10 cycles indicate that BTO@Ti/Li-BTO@Ti/Li battery possesses the minimum impedance (Figure S6), which is in accordance with the results in Figure 5c. To evaluate the electrochemical performance of nBTO@Ti/Li symmetric battery at higher current densities, charge-discharge current densities were successively increased from 0.5 mA cm^{-2} to 1 mA cm^{-2} and 2 mA cm^{-2} at a constant capacity of 0.5 mAh cm^{-2} (Figures 5d and S7). Compared to BTO@Ti/Li and Ti/Li, nBTO@Ti/Li consistently shows the flattest potential platforms and the lowest overpotentials of 25 mV at 0.5 mA cm^{-2}, 40 mV at 1 mA cm^{-2} and 60 mV at 2 mA cm^{-2} (Table 1). The overpotentials for BTO@Ti/Li at 0.5 mA cm^{-2}, 1 mA cm^{-2}, and 2 mA cm^{-2} are 30 mV, 50 mV, and 80 mV, respectively, while the overpotentials for Ti/Li are 40 mV, 60 mV, and 100 mV, respectively. Li-LiFePO$_4$ full cells with LiFePO$_4$ as cathode were tested at 1 C to further study the electrochemical performance of nBTO@Ti/Li. Full cells with nBTO@Ti/Li as anode exhibit a stable discharge-specific capacity of 120 mAh g^{-1} and a capacity retention rate of 93.3% after 200 cycles (Figure 5e). When BTO@Ti/Li and Ti/Li electrodes are used as anodes, the specific discharge capacities decrease rapidly with cycling. Voltage profiles of the Li-LFP full cells with different anodes can be seen in Figure S8. When nBTO@Ti/Li is applied as an anode, stable charge–discharge curves with a minimum difference of potential plateau (80 mV) are achieved. By contrast, BTO@Ti/Li-LiFePO$_4$ and Ti/Li-LiFePO$_4$ full cells exhibit larger differences in potential plateaus and significant capacity fading after 100 cycles.

Table 1. Overpotentials of symmetric batteries at different current densities.

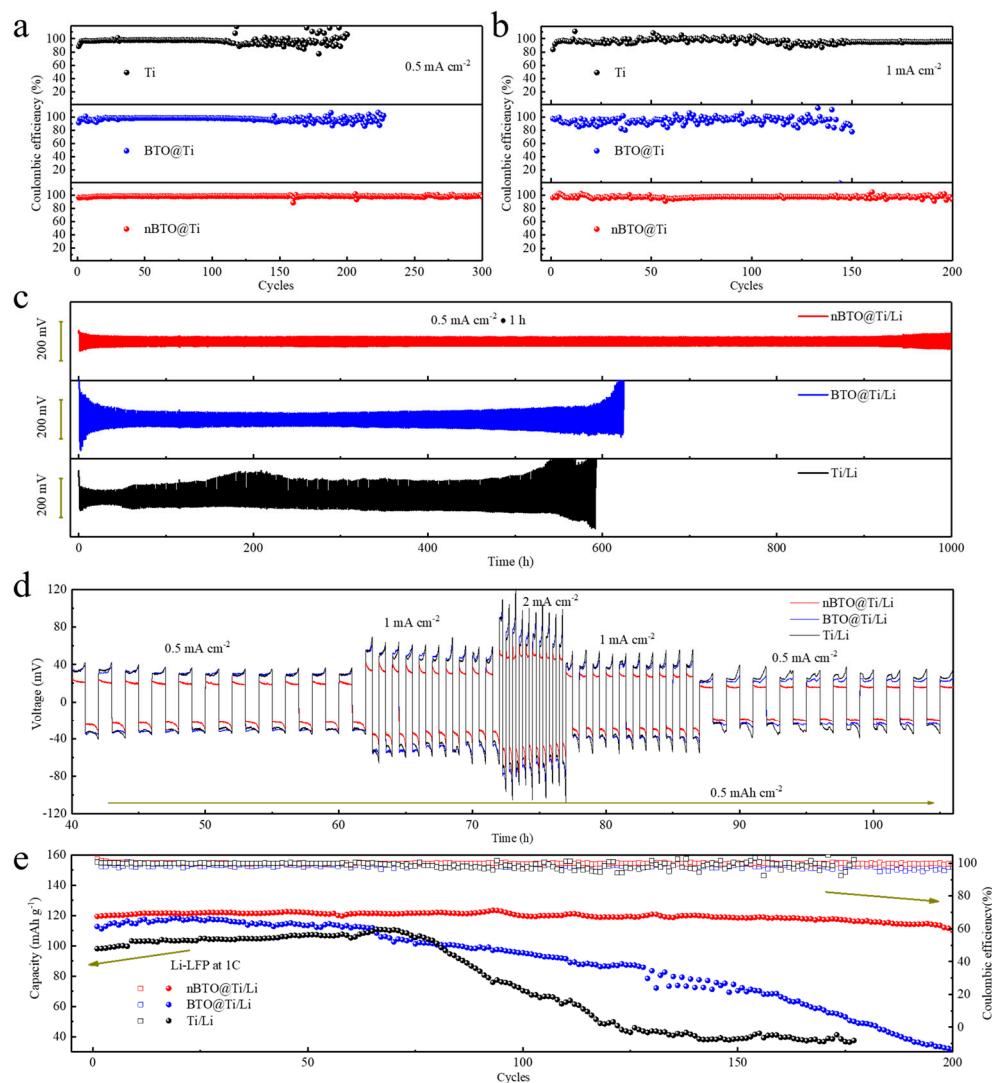| Current Densities	0.5 mA cm^{-2}	1 mA cm^{-2}	2 mA cm^{-2}
nBTO@Ti/Li	25 mV	40 mV	60 mV
BTO@Ti/Li	30 mV	50 mV	80 mV
Ti/Li	40 mV	60 mV	100 mV

Figure 5. Coulombic efficiency of nBTO@Ti, BTO@Ti and Ti electrodes at (**a**) 0.5 mA cm^{-2}, 0.5 mAh cm^{-2} and (**b**) 1 mA cm^{-2}, 0.5 mAh cm^{-2}. Electrochemical performances of symmetric cells at (**c**) 0.5 mA cm^{-2} and (**d**) different current densities. (**e**) Discharge capacities and CEs of Li-LiFePO$_4$ full cells at 1 C.

4. Conclusions

In summary, a polarized BaTiO$_3$ dipole layer is proposed to guide uniform lithium nucleation and subsequent plating process in this work. The orientation of polarized BaTiO$_3$ dipoles in BTO film is verified via UPS and ferroelectric hysteresis loops. Simulation results of finite element modeling indicate that the extra electrostatic potential can markedly increase the Li-ion concentration near nBTO@Ti and modify the diffused double layer. As a result, the energy barrier of lithium nucleation on nBTO@Ti is significantly decreased, and a high average CE of 98.3% is achieved during 300 cycles at 0.5 mA cm^{-2}. SEM further investigated the stable nucleation and plating processes of lithium on nBTO@Ti in different stages. The electrochemical performances of symmetrical cells and full cells with nBTO@Ti/Li electrodes are obviously improved. Such a strategy can also be applied in other metal batteries to regulate the nucleation stage and increase the stability of the plating process.

(a) Ba 3d, (b) Ti 2p, and (c) O 1s XPS spectra of BTO@Ti foil. Figure S4: UPS pattern of pBTO@Ti foil. Figure S5: Amplifications of Figure 5c at different stages. Figure S6: Nyquist plots of the symmetric cells after 10 cycles. Figure S7: Amplifications of Figure 5d at different current densities. (a) 0.5 mA cm^{-2}. (b) 1 mA cm^{-2}. (c) 2 mA cm^{-2}. Figure S8: Voltage profiles of the Li-LiFePO$_4$ full cell at 1C. (a) nBTO@Ti/Li. (b) BTO@Ti/Li. (c) Ti/Li.

References

1. Zou, P.; Sui, Y.; Zhan, H.; Wang, C.; Xin, H.L.; Cheng, H.M.; Kang, F.; Yang, C. Polymorph Evolution Mechanisms and Regulation Strategies of Lithium Metal Anode under Multiphysical Fields. *Chem. Rev.* **2021**, *121*, 5986–6056. [CrossRef] [PubMed]
2. Wang, Q.; Wang, H.; Wu, J.; Zhou, M.; Liu, W.; Zhou, H. Advanced electrolyte design for stable lithium metal anode: From liquid to solid. *Nano Energy* **2021**, *80*, 105516. [CrossRef]
3. Shi, Y.; Li, B.; Zhang, Y.; Cui, Y.; Cao, Z.; Du, Z.; Gu, J.; Shen, K.; Yang, S. Tortuosity Modulation toward High-Energy and High-Power Lithium Metal Batteries. *Adv. Energy Mater.* **2021**, *11*, 2003663. [CrossRef]
4. Xu, G.; Li, J.; Wang, C.; Du, X.; Lu, D.; Xie, B.; Wang, X.; Lu, C.; Liu, H.; Dong, S.; et al. The Formation/Decomposition Equilibrium of LiH and its Contribution on Anode Failure in Practical Lithium Metal Batteries. *Angew. Chem. Int. Ed.* **2021**, *60*, 7770–7776. [CrossRef]
5. Shen, X.; Zhang, R.; Shi, P.; Chen, X.; Zhang, Q. How Does External Pressure Shape Li Dendrites in Li Metal Batteries? *Adv. Energy Mater.* **2021**, *11*, 2003416. [CrossRef]
6. Zhang, S. Suppressing Li Dendrites via Electrolyte Engineering by Crown Ethers for Lithium Metal Batteries. *Nano-Micro Letters* **2020**, *12*, 158. [CrossRef]
7. Zhang, L.; Yang, T.; Du, C.; Liu, Q.; Tang, Y.; Zhao, J.; Wang, B.; Chen, T.; Sun, Y.; Jia, P.; et al. Lithium whisker growth and stress generation in an in situ atomic force microscope-environmental transmission electron microscope set-up. *Nat. Nanotechnol.* **2020**, *15*, 94–98. [CrossRef]
8. Du, P.; Li, B.; Mao, Z.; Nan, Y.; Cuo, D.; Wu, S. Regulating lithium-ion flow by piezoelectric effect of the poled-BaTiO3 film for dendrite-free lithium metal anode. *J. Electroanal. Chem.* **2022**, *919*, 116538. [CrossRef]
9. Zhou, T.; Zhao, Y.; El Kazzi, M.; Choi, J.W.; Coskun, A. Stable Solid Electrolyte Interphase Formation Induced by Monoquat-Based Anchoring in Lithium Metal Batteries. *ACS Energy Lett.* **2021**, *6*, 1711–1718. [CrossRef]
10. Zhai, P.; Liu, L.; Wei, Y.; Zuo, J.; Yang, Z.; Chen, Q.; Zhao, F.; Zhang, X.; Gong, Y. Self-Healing Nucleation Seeds Induced Long-Term Dendrite-Free Lithium Metal Anode. *Nano Lett.* **2021**, *21*, 7715–7723. [CrossRef]
11. Yang, D.; Zhao, C.; Lian, R.; Yang, L.; Wang, Y.; Gao, Y.; Xiao, X.; Gogotsi, Y.; Wang, X.; Chen, G.; et al. Mechanisms of the Planar Growth of Lithium Metal Enabled by the 2D Lattice Confinement from a Ti$_3$C$_2$T$_x$ MXene Intermediate Layer. *Adv. Funct. Mater.* **2021**, *31*, 2010987. [CrossRef]
12. Wang, K.; Li, X.; Gao, J.; Sun, Q.; Yang, Z.; He, J.; Cui, S.; Huang, C. Self-Regulation Seaweed-Like Lithium Metal Anode Enables Stable Cycle Life of Lithium Battery. *Adv. Funct. Mater.* **2021**, *31*, 2009917. [CrossRef]
13. Zhang, X.; Chen, Y.; Yu, B.; Wang, B.; Wang, X.; Zhang, W.; Yang, D.; He, J. Lithiophilic 3D VN@N-rGO as a Multifunctional Interlayer for Dendrite-Free and Ultrastable Lithium-Metal Batteries. *ACS Appl. Mater. Interfaces* **2021**, *13*, 20125–20136. [CrossRef]
14. Zhai, P.; Wang, T.; Jiang, H.; Wan, J.; Wei, Y.; Wang, L.; Liu, W.; Chen, Q.; Yang, W.; Cui, Y.; et al. 3D Artificial Solid-Electrolyte Interphase for Lithium Metal Anodes Enabled by Insulator-Metal-Insulator Layered Heterostructures. *Adv. Mater.* **2021**, *33*, 2006247. [CrossRef]
15. Chen, X.R.; Zhao, B.C.; Yan, C.; Zhang, Q. Review on Li Deposition in Working Batteries: From Nucleation to Early Growth. *Adv. Mater.* **2021**, *33*, 2004128. [CrossRef]
16. Guan, X.; Wang, A.; Liu, S.; Li, G.; Liang, F.; Yang, Y.W.; Liu, X.; Luo, J. Controlling Nucleation in Lithium Metal Anodes. *Small* **2018**, *14*, 1801423. [CrossRef]
17. Xu, Y.; Gao, L.; Shen, L.; Liu, Q.; Zhu, Y.; Liu, Q.; Li, L.; Kong, X.; Lu, Y.; Wu, H.B. Ion-Transport-Rectifying Layer Enables Li-Metal Batteries with High Energy Density. *Matter* **2020**, *3*, 1685–1700. [CrossRef]
18. Pei, A.; Zheng, G.; Shi, F.; Li, Y.; Cui, Y. Nanoscale Nucleation and Growth of Electrodeposited Lithium Metal. *Nano Lett.* **2017**, *17*, 1132–1139. [CrossRef] [PubMed]
19. Meng, J.; Li, C. Planting CuGa$_2$ seeds assisted with liquid metal for selective wrapping deposition of lithium. *Energy Storage Mater.* **2021**, *37*, 466–475. [CrossRef]

20. Liu, T.; Chen, S.; Sun, W.; Lv, L.P.; Du, F.H.; Liu, H.; Wang, Y. Lithiophilic Vertical Cactus-Like Framework Derived from Cu/Zn-Based Coordination Polymer through In Situ Chemical Etching for Stable Lithium Metal Batteries. *Adv. Funct. Mater.* **2021**, *31*, 2008514. [CrossRef]

21. Zhu, M.; Zhang, J.; Ma, Y.; Nan, Y.; Li, S. Guiding confined deposition of lithium through the conductivity changing interface within a hierarchical heterostructure toward dendrite-free lithium anodes. *Carbon* **2020**, *168*, 633–639. [CrossRef]

22. Zou, P.; Wang, C.; Qin, J.; Zhang, R.; Xin, H.L. A reactive wetting strategy improves lithium metal reversibility. *Energy Storage Mater.* **2023**, *58*, 176–183. [CrossRef]

23. Chen, Y.; Li, M.; Liu, Y.; Jie, Y.; Li, W.; Huang, F.; Li, X.; He, Z.; Ren, X.; Chen, Y.; et al. Origin of dendrite-free lithium deposition in concentrated electrolytes. *Nat. Commun.* **2023**, *14*, 2655. [CrossRef] [PubMed]

24. Fang, Y.; Zeng, Y.; Jin, Q.; Lu, X.F.; Luan, D.; Zhang, X.; Lou, X.W.D. Nitrogen-Doped Amorphous Zn-Carbon Multichannel Fibers for Stable Lithium Metal Anodes. *Angew. Chem. Int. Ed.* **2021**, *60*, 8515–8520. [CrossRef] [PubMed]

25. Dong, K.; Xu, Y.; Tan, J.; Osenberg, M.; Sun, F.; Kochovski, Z.; Pham, D.T.; Mei, S.; Hilger, A.; Ryan, E.; et al. Unravelling the Mechanism of Lithium Nucleation and Growth and the Interaction with the Solid Electrolyte Interface. *ACS Energy Lett.* **2021**, *6*, 1719–1728. [CrossRef]

26. Liu, S.; Ma, Y.; Zhou, Z.; Lou, S.; Huo, H.; Zuo, P.; Wang, J.; Du, C.; Yin, G.; Gao, Y. Inducing uniform lithium nucleation by integrated lithium-rich li-in anode with lithiophilic 3D framework. *Energy Storage Mater.* **2020**, *33*, 423–431. [CrossRef]

27. Haslam, C.; Sakamoto, J. Stable Lithium Plating in "Lithium Metal-Free" Solid-State Batteries Enabled by Seeded Lithium Nucleation. *J. Electrochem. Soc.* **2023**, *170*, 040524. [CrossRef]

28. Nan, Y.; Li, S.; Shi, Y.; Yang, S.; Li, B. Gradient-Distributed Nucleation Seeds on Conductive Host for a Dendrite-Free and High-Rate Lithium Metal Anode. *Small* **2019**, *15*, 1903520. [CrossRef]

29. Lin, Y.; Qian, Q.; Chen, Z.; Dinh Tuan, P.; Feng, D. Fabrication of high specific surface area TiO_2 nanopowders by anodization of porous titanium. *Electrochem. Commun.* **2022**, *136*, 107234. [CrossRef]

30. Yim, T.; Han, S.H.; Park, N.H.; Park, M.-S.; Lee, J.H.; Shin, J.; Choi, J.W.; Jung, Y.; Jo, Y.N.; Yu, J.-S.; et al. Effective Polysulfide Rejection by Dipole-Aligned $BaTiO_3$ Coated Separator in Lithium-Sulfur Batteries. *Adv. Funct. Mater.* **2016**, *26*, 7817–7823. [CrossRef]

31. Zhang, Y.; Zhao, X.; Chen, J.; Li, S.; Yang, W.; Fang, X. Self-Polarized $BaTiO_3$ for Greatly Enhanced Performance of ZnO UV Photodetector by Regulating the Distribution of Electron Concentration. *Adv. Funct. Mater.* **2019**, *30*, 1907650. [CrossRef]

32. Xia, M.; Yi-ran, L.; Xiong, X.; Hu, W.; Tang, Y.-w.; Zhou, N.; Zhou, Z.; Zhang, H.-b. Enhancing the electrochemical performance of micron-scale SiO@C/CNTs anode via adding piezoelectric material $BaTiO_3$ for high-power lithium ion battery. *J. Alloys Compd.* **2019**, *800*, 116–124. [CrossRef]

33. Alluri, N.R.; Purusothaman, Y.; Chandrasekhar, A.; Kim, S.-J. Self-powered wire type UV sensor using in-situ radial growth of $BaTiO_3$ and TiO_2 nanostructures on human hair sized single Ti-wire. *Chem. Eng. J.* **2018**, *334*, 1729–1739. [CrossRef]

34. Wang, C.; Li, Y.; Yao, Z.; Kim, H.-J.; Kim, N.-Y. Characteristics and mechanisms of aerosol deposition-based barium titanate by sulfur hexafluoride inductively coupled plasma etching. *Mater. Sci. Semicond. Process.* **2015**, *30*, 388–392. [CrossRef]

35. Wang, H.; Guo, Z.; Hao, W.; Sun, L.; Zhang, Y.; Cao, E. Ethanol sensing characteristics of $BaTiO_3/LaFeO_3$ nanocomposite. *Mater. Lett.* **2019**, *234*, 40–44. [CrossRef]

36. Chrzanowski, J.; Matuszak, M. The double dipole layer and work function of metals. *Appl. Surf. Sci.* **2020**, *527*, 146767. [CrossRef]

37. Xue, M.; Xie, J.; Li, W.; Wang, F.; Ou, J.; Yang, C.; Li, C.; Zhong, Z.; Jiang, Z. Changes in surface morphology and work function caused by corrosion in aluminum alloys. *J. Phys. Chem. Solids* **2012**, *73*, 781–787. [CrossRef]

38. Krzeszewski, M.; Espinoza, E.M.; Cervinka, C.; Derr, J.B.; Clark, J.A.; Borchardt, D.; Beran, G.J.O.; Gryko, D.T.; Vullev, V.I. Dipole Effects on Electron Transfer are Enormous. *Angew. Chem. Int. Ed.* **2018**, *57*, 12365–12369. [CrossRef]

39. Chen, K.-H.; Wood, K.N.; Kazyak, E.; LePage, W.S.; Davis, A.L.; Sanchez, A.J.; Dasgupta, N.P. Dead lithium: Mass transport effects on voltage, capacity, and failure of lithium metal anodes. *J. Mater. Chem. A* **2017**, *5*, 11671–11681. [CrossRef]